Research Article | Open Access

Microstructures

Zhou *et al*. *Microstructures* **2026**, *6*, 2026029 **DOI:**10.20517/microstructures.2025.101

Impact of grain boundary segregation on piezoelectric performance of $CaBi_2Nb_2O_9$ high-temperature piezoceramics

Yangyang Zhou[1,2], **Yanyan Zhang**[1,2], **Jianfeng Huang**[1,2], **Runlin Liu**[3], **Zhengqian Fu**[1], **Fangfang Xu**[1], **Zhonghui Shen**[3], **Ruihong Liang**[1], **Zhiyong Zhou**[1]

Keywords: High-temperature piezoelectric ceramics, grain boundary segregation, domain switching, internal stress, fracture toughness

Citation: Zhou, Y.; Zhang, Y.; Huang, J.; Liu, R.; Fu, Z.; Xu, F.; Shen, Z.; Liang, R.; Zhou, Z. Impact of grain boundary segregation on piezoelectric performance of $CaBi_2Nb_2O_9$ high-temperature piezoceramics. *Microstructures* **2026**, *6*, 2026029. https://dx.doi.org/10.20517/microstructures.2025.101

Received: 14 Jul 2025
First Decision: 14 Aug 2025
Revised: 23 Aug 2025
Accepted: 2 Sep 2025
Published: 13 Mar 2026

Academic Editor: Jing-Feng Li
Copy Editor: Fangling Lan
Production Editor: Fangling Lan

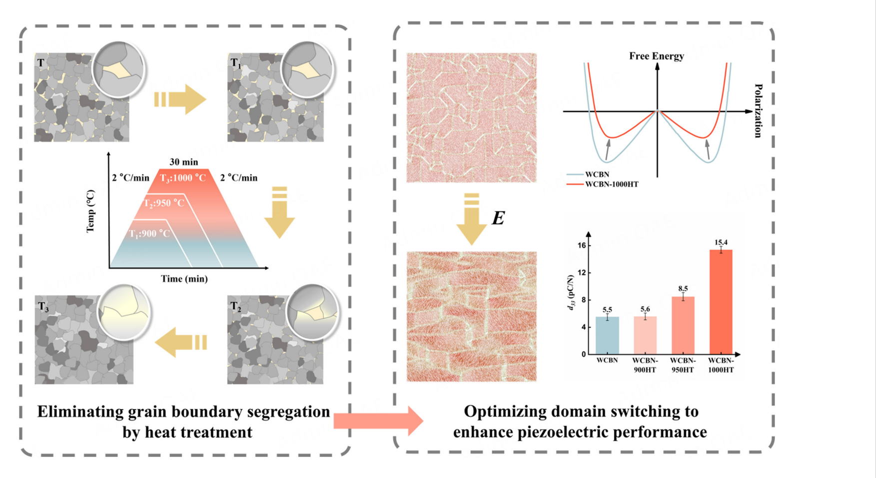

Abstract

Grain boundary segregation plays a critical role in determining the properties of polycrystalline materials, yet its influence on piezoelectric performance remains underexplored. In this work, bismuth layer-structured piezoceramic W^{6+}-doped $CaBi_2Nb_2O_9$ (WCBN) was chosen to investigate the effect of grain boundary segregation on the piezoelectric properties through multiscale structural characterization and phase-field simulations. The results reveal that improper grain boundary segregation can induce internal stress fields that restrict domain switching dynamics, leading to deterioration of the piezoelectric response. Therefore, a novel poling process was developed, which effectively alleviated the segregation-induced stress constraints and enhanced the piezoelectric coefficients by 180%. More importantly, optimizing the preparation process significantly enhances the mechanical properties, particularly increasing the fracture toughness of WCBN ceramics to 2.73 MPa $m^{1/2}$, which is more than twice that of traditional $Pb(Zr, Ti)O_3$ piezoceramics. These findings establish direct correlations between grain

---

[1]State Key Laboratory of High Performance Ceramics and Superfine Microstructures, Shanghai Institute of Ceramics, Chinese Academy of Sciences, Shanghai 200050, China.
[2]Center of Materials Science and Optoelectronics Engineering, University of Chinese Academy of Sciences, Beijing 100049, China.
[3]State Key Laboratory of Advanced Technology for Materials Synthesis and Processing, Center of Smart Materials and Devices, Wuhan University of Technology, Wuhan 430070, Hubei, China.

Correspondence to: Prof. Zhiyong Zhou, State Key Laboratory of High Performance Ceramics and Superfine Microstructures, Shanghai Institute of Ceramics, Chinese Academy of Sciences, 585 Heshuo Road, Shanghai 200050, China. E-mail: zyzhou@mail.sic.ac.cn

boundary segregation, internal stress, and domain switching behavior, providing fundamental insights for the design of piezoelectric materials that integrate both high piezoelectric and mechanical properties, which could be greatly beneficial to long-term stable operation in harsh environments with high temperatures and complex vibrations for bismuth layer-structured piezoceramics.

INTRODUCTION

Grain boundary segregation significantly influences the properties and performance of polycrystalline materials during service. The selective enrichment of solute atoms at grain boundaries can facilitate the formation of functional interfacial phases, thereby enhancing material performance[1-4]. For example, in (Nb, Ba)-doped TiO_2 ceramics, the segregation of Ba^{2+} ions at grain boundaries introduces localized transport barriers, enabling lower-voltage operation in TiO_2 varistors[2]. In addition, in Nd-Fe-B-based magnets, the segregation of Nd and Cu has been shown to enhance domain wall pinning strength, resulting in a significant increase in the coercive field[4,5]. On the other hand, the microstructural inhomogeneity induced by grain boundary segregation can also inevitably deteriorate material properties. Specifically, in Mo-based alloys, oxygen segregation at grain boundaries reduces grain boundary cohesion, increasing the risk of embrittlement[6]. Similarly, the segregation of Al and O at grain boundaries in SiC ceramics reduces grain boundary scattering, resulting in a significant decrease in thermal conductivity[7]. The differences that cause this change in material properties are directly related to the structure and composition of the grain boundary complexions formed by segregation.

Piezoelectric materials, which enable the interconversion between mechanical and electrical energies, have been widely applied in various fields ranging from consumer electronics to high-end industries[8-12]. Over the past few decades, ionic doping has been extensively employed in various piezoelectric materials to enhance their piezoelectric properties[13-16]. For example, Li *et al.* achieved an ultrahigh piezoelectric coefficient of 1,500 pC/N in Sm-doped $Pb(Mg_{1/3}Nb_{2/3})O_3$-$PbTiO_3$ ceramics[14]. However, it is noteworthy that much attention has been paid to the impact of dopant ions incorporated into the crystal lattice on piezoelectric properties, which leads to the fact that investigations about the grain boundary segregation in piezoelectric materials remain relatively scarce, and how grain boundary segregation influences piezoelectric performance is still unclear[17,18]. Therefore, understanding how grain boundary segregation affects piezoelectric material performance and how to eliminate it at the atomic scale is of great importance to modulating materials' properties through grain boundary composition and structure.

Bismuth layer-structured piezoceramics (BLSPs) with high Curie temperatures (T_C) are widely used in high-temperature environments such as aerospace and nuclear power industries. Among the reported BLSP materials, $CaBi_2Nb_2O_9$ (CBN) exhibits the highest Curie temperature (T_C ~ 943 °C) coupled with high resistivity, making it one of the most promising candidates for high-temperature applications (above 600 °C)[19,20]. However, in BLSPs, the perovskite-like layers (e.g., $(CaNb_2O_7)^{2-}$ layers in CBN) and $(Bi_2O_2)^{2+}$ layers are intergrown, and the lateral dimensional mismatch between them causes structural instability in both types of layers[21]. This instability restricts the allowable range of the tolerance factor and makes grain boundary segregation more likely to occur. Therefore, this study selected CBN as the matrix material and doped equivalent W^{6+} ions (WCBN). By combining multi-scale structural characterization with phase-field simulation, we systematically investigated how grain boundary segregation affects piezoelectric properties through the modulation of the microstructure. Furthermore, by optimizing the ceramic preparation and poling processes, the mechanical and piezoelectric properties of WCBN ceramics were further enhanced.

These results provide fundamental guidelines for understanding the action mechanism of grain boundary segregation and designing piezoelectric ceramics with high piezoelectric and mechanical performance, paving the way for practical applications.

MATERIALS AND METHODS

Sample preparation

$CaBi_2Nb_{1.975}W_{0.025}O_9$ (WCBN) ceramics were prepared by the conventional solid-phase reaction method using Bi_2O_3 (99.9%, Golden Time Chemical (Jiangsu) Co., Ltd., China), Nb_2O_5 (99.9%, Zhuzhou Chenchang Metal Co., Ltd., China), $CaCO_3$ (99%, Aladdin Biochemical Technology Co., Ltd., China), and WO_3 (99%, Sinopharm Chemical Reagent Co., Ltd., China) as raw materials. Firstly, the initial raw materials were ball-milled in an alcoholic grinding medium for 4 h, dried, and then calcined at 850 °C for 2 h. The calcined powder was ball-milled again for 6 h and then pressed into discs with a diameter of 13 mm and a thickness of 1 mm. The ceramic green bodies formed via isostatic pressing were sintered at 1,100-1,150 °C for 2 h in an oxygen atmosphere. All ceramic samples were poled in a silicone oil bath under a direct current electric field of 16 kV/mm at 200 °C for 10 min for piezoelectric properties measurement. The heat treatment process involved heating the prepared ceramics to 900-1000 °C at a rate of 2 °C/min, holding for 30 min, followed by cooling to room temperature at the same rate (2 °C/min).

Structure characterization

High-resolution X-ray diffraction (HR-XRD, D8 Discover Davinci, Bruker, Germany) was used to measure the internal stress of ceramics. Synchrotron X-ray diffraction (synchrotron XRD) was performed on WCBN and WCBN-1000HT at the Australian Synchrotron using an incident X-ray wavelength of 1.00065 Å (12.4 keV) to determine the crystal structure. Transmission electron microscopy (TEM, JEM-2100F, JEOL, Japan) was used to investigate the microstructure of the sample. Strain analysis of the High-resolution TEM (HR-TEM) was carried out by using the commercial Geometric Phase Analysis package by HREM Research. Annular bright-field (ABF) scanning transmission electron microscopy (STEM, Titan Themis Z, FEI, USA) images, as well as EDS mapping, were obtained using an advanced STEM system. Microstructural analysis was performed using a scanning electron microscope (SEM, Hitachi, Tokyo, Japan) equipped with an energy-dispersive X-ray spectrometer (EDS, Oxford, England) and an electron backscatter diffraction (EBSD, Home developed). Electron channeling contrast imaging (ECCI) images can be obtained accordingly. The elemental distributions of the polished samples were characterized using an electron probe X-ray micro-analyzer (EPMA, JXA-Ihp200f, JEOL, Japan). X-ray photoelectron spectroscopy (XPS, Escalab 250Xi, ThermoFisher) was used to analyze the oxygen vacancy concentration. Piezoelectric force microscopy (PFM) measurements were performed on a commercial Atomic Force Microscope system (AFM, Jupiter XR, Oxford, UK).

Ex-situ electric field XRD

XRD was carried out using a Panalytical Aeris diffractometer with Cu Kα radiation in the 2θ range of 10°-90° with a step size of 0.003° and 50 s per step. Since macroscopic domain switching cannot be fully achieved in WCBN and WCBN-1000HT ceramics at room temperature, and *in situ* electric field XRD is not feasible under high-temperature conditions, *ex-situ* electric field XRD was employed. The specific testing procedure was as follows: Circular Au electrodes (7 mm in diameter) were deposited onto the ceramic surface using a stainless-steel shadow mask. After applying different electric fields in a 200 °C silicone oil bath, one of the electrodes was removed by polishing with 1500-grit sandpaper, followed by XRD measurement, and this process was repeated cyclically.

Property characterization

The DC resistance was characterized by employing a high-resistance measurement system (Model HRMS-1000, Partulab, Wuhan, China). The dielectric constant was measured from 50 to 980 °C using an impedance material analyzer (DMS-1000, Partulab, China) and a meter (Model E4990A; Keysight, USA).

The d_{33} was measured with a d_{33} meter (Model ZJ-3; Institute of Acoustics) for samples subjected to heat treatment at different temperatures (for each type of ceramic, ten specimens were tested for d_{33} , with five different positions measured on each specimen, and the average value was calculated.). The fracture toughness K_{IC} was determined using the following equation:

$$K_{\mathrm{IC}} = 0.018\left(\frac{E}{H_{\mathrm{V}}}\right)^{0.4} H_{\mathrm{V}} a^{1/2}\left(\frac{l}{a}\right)^{-0.5} \tag{1}$$

where E is the Young's modulus, H_V is the Vickers-hardness, a is half of the indentation length, and l is the length of the VIF-induced crack. The high-temperature fracture toughness test was conducted using the following parameters: a heating rate of 10 °C/min, a holding time of 10 min, and a loading rate of 0.05 mm/min.

Internal stress analysis

The internal stress in ceramics can be calculated using the $\sin^2\psi$ method, as described by the following equation:

$$\sigma_x = \frac{E}{2(1+v)} cot\theta_0 \frac{\pi}{180}\left(\frac{\partial 2\theta}{\partial \sin^2\psi}\right) \tag{2}$$

where θ_0 is the Bragg's angle at the diffraction peak without residual stress, θ is Bragg's angle with residual stress, ψ is the tilting angle, E is the elastic modulus, and v is the Poisson's ratio. In this work, the elastic modulus was set to 130 GPa, and the Poisson's ratio to 0.3.

RESULTS AND DISCUSSION

To reduce the risk of device failure caused by piezoelectric ceramics fracture at high temperatures, an optimized solid-phase reaction method was carried out to fabricate WCBN ceramics. This process substitutes conventional uniaxial pressing with isostatic pressing while achieving ceramic densification through a combined high oxygen partial pressure sintering environment. Figure 1A and B shows the SEM images and statistical grain size distribution data of WCBN ceramics. The results indicate that WCBN ceramics exhibit a homogeneous microstructure with high densification (relative density exceeding 99%), and no obvious pores were observed. Furthermore, evaluation of piezoelectric ceramics' resistance to high-temperature fragmentation through fracture toughness testing revealed that WCBN ceramics display an excellent room-temperature fracture toughness of 2.73 MPa·m$^{1/2}$, which is two times that of traditional PZT piezoceramics and remains at 2.40 MPa·m$^{1/2}$ even under 600 °C conditions [Figure 1C]. This performance is significantly superior to that of reported piezoelectric ceramic systems [Figure 1D], demonstrating its potential for long-term service in high-temperature devices.

To verify the compositional distribution of the W element, ECCI combined with EDS was first employed. After mechanical polishing and etching, the ECCI image of the WCBN ceramics surface reveals a significant amount of bright contrast from the secondary phase [Figure 2A]. Notably, this phase is also observed in cross-sectional views of the WCBN ceramics, which excludes the possibility that the secondary phase is only present on the surface [Supplementary Figure 1]. Line-scan profiling across the secondary phase in the ECCI image indicates that it results from the segregation of doped W and Bi elements [Figure 2A]. The HR-TEM image of lattice fringes in Figure 2B shows good crystal quality, indicating that the secondary phase is a crystalline phase rather than an amorphous phase. Furthermore, compositional distribution was further

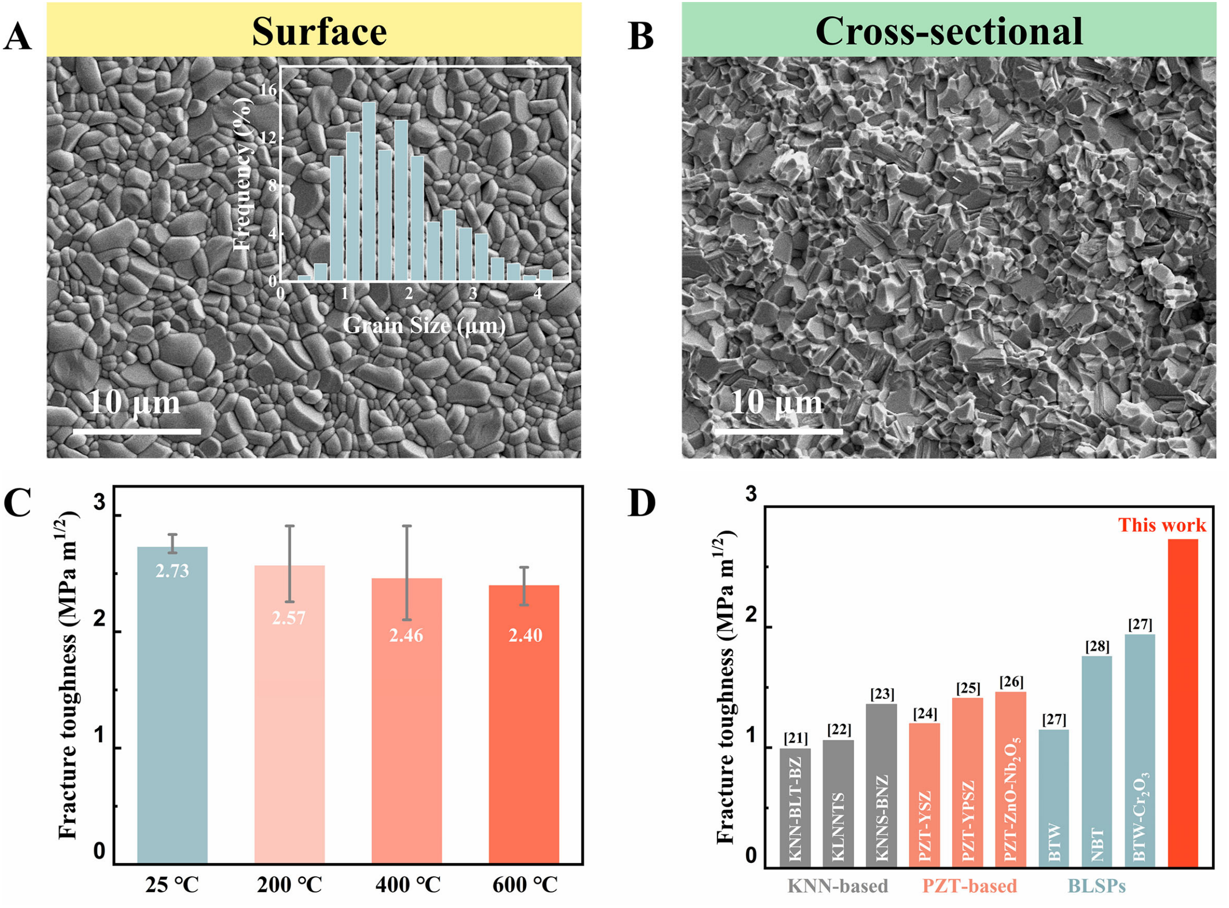

Figure 1. SEM images of WCBN ceramics (A) surface and (B) cross-section. (C) Temperature-dependent fracture toughness of WCBN ceramics. (D) Fracture toughness in this work and other reported piezoelectric ceramics[22-29].

examined through STEM and EPMA testing at higher resolution. The experiment results are consistent with ECCI-EDS, showing significant segregation of W and Bi elements [Figure 2C and Supplementary Figure 2]. This phenomenon of grain boundary segregation is different from the previously reported penetration of dopant ions into the lattice of BLSPs[30-33]. The lack of understanding of the grain boundary complex of BLSFPs seriously restricts the design of high-performance piezoelectric materials.

Grain boundaries serve as the most active regions in a material's microstructure. Changes in their interfacial states may affect the nucleation and growth of ferroelectric domains, thereby influencing piezoelectric performance[34,35]. This is evidenced in the macroscopic piezoelectric response, where the d_{33} reaches only 5.5 pC/N under a high polarization electric field of 16 kV/mm. At this moment, the PFM phase image reveals that a significant number of domain structures remain unswitched [Supplementary Figure 3], indicating that the WCBN ceramics are still far from saturated polarization. Based on these findings, this work proposes a rational hypothesis: grain boundary segregation may suppress domain switching, thereby compromising piezoelectric performance.

According to Fick's Second Law of Diffusion and Arrhenius equation, the diffusion rate of ions $D = D_0 e^{-\frac{Ea}{RT}}$ positively correlates with temperature. As the temperature increases, the solubility of WCBN ceramics increases, and W^{6+} ions that segregate to the grain boundary are more easily moved into the grain [Figure 3A]. Therefore, a novel and interesting poling process was adopted involving high-temperature pre-treatment coupled with poling to mitigate grain boundary segregation, thereby enhancing the

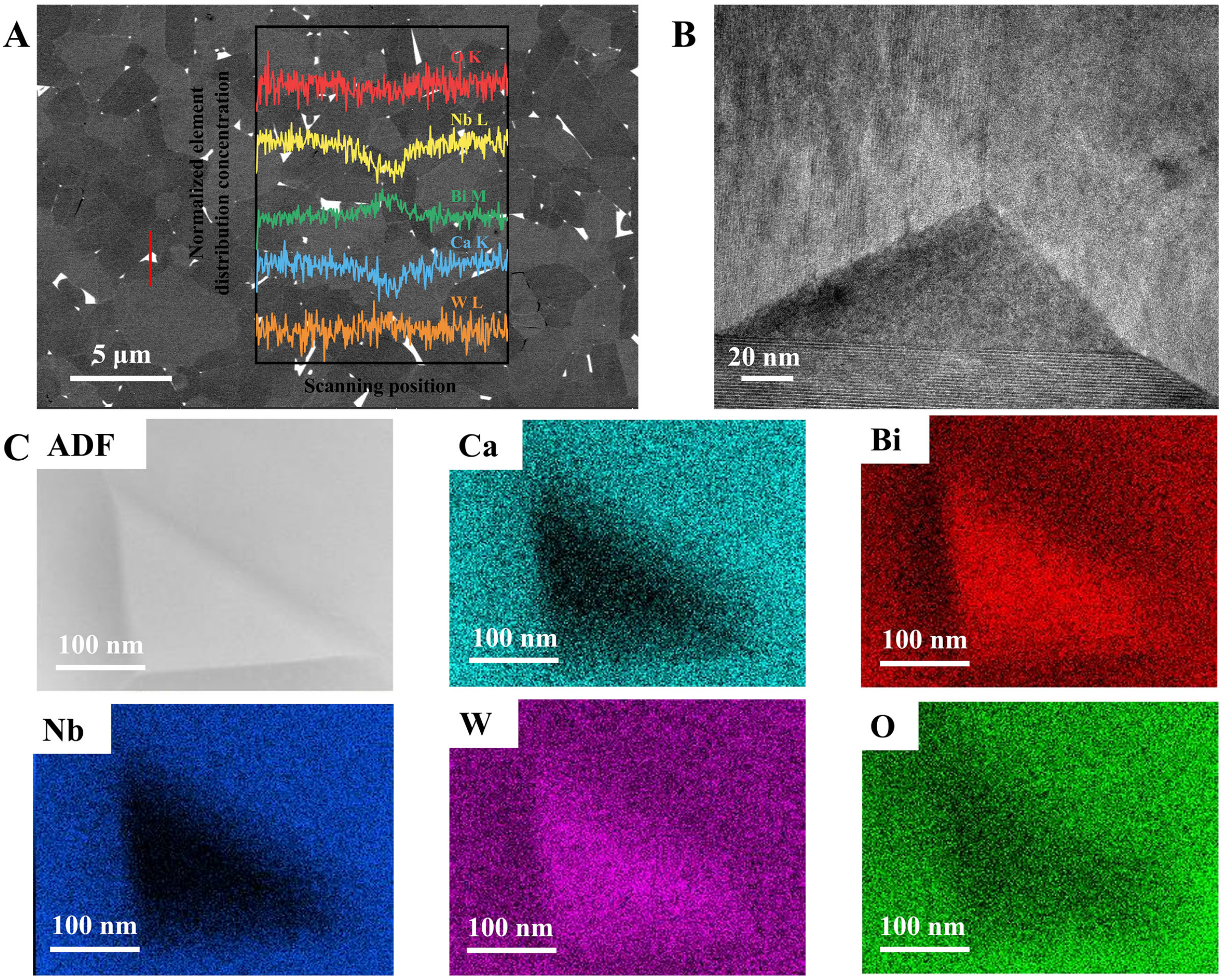

Figure 2. (A) ECCI image of the surface of WCBN ceramics. (B) TEM image at triangular grain boundaries. (C) Element concentration distribution at triangular grain boundaries.

piezoelectric properties. To control the grain boundary segregation in WCBN ceramics, a specific heat treatment process was established with temperatures of T_1 (900 °C), T_2 (950 °C), and T_3 (1,000 °C), designated as WCBN-900HT, WCBN-950HT, and WCBN-1000HT, respectively.

Figure 3B presents the ECCI images of the surface of WCBN ceramics after heat treatment at different temperatures (the cross-sectional ECCI images were provided in Supplementary Figure 4). The secondary phase at the grain boundaries is indicated with red and quantified using ImageJ software as shown in Figure 3C. It can be seen that the grain boundary characteristics undergo significant changes after heat treatment. As the heat treatment temperature increases, the secondary phase at the grain boundaries gradually diminishes. After poling the WCBN, WCBN-900HT, WCBN-950HT, and WCBN-1000HT ceramics, it was found that the d_{33} gradually increased with the increase of heat treatment temperature. Compared to WCBN ceramics, WCBN-1000HT ceramics exhibit an increase in d_{33} value of 15.4 pC/N, which is more than 180% and retain 90% of their room-temperature d_{33} after annealing at 900 °C, demonstrating excellent thermal stability [Figure 3D and E]. Surprisingly, the piezoelectric coefficient after heat treatment at different temperatures exhibits a strong negative correlation with the content of the secondary phase at the grain boundaries. This result strongly supports that excessive grain boundary segregation can deteriorate piezoelectric properties.

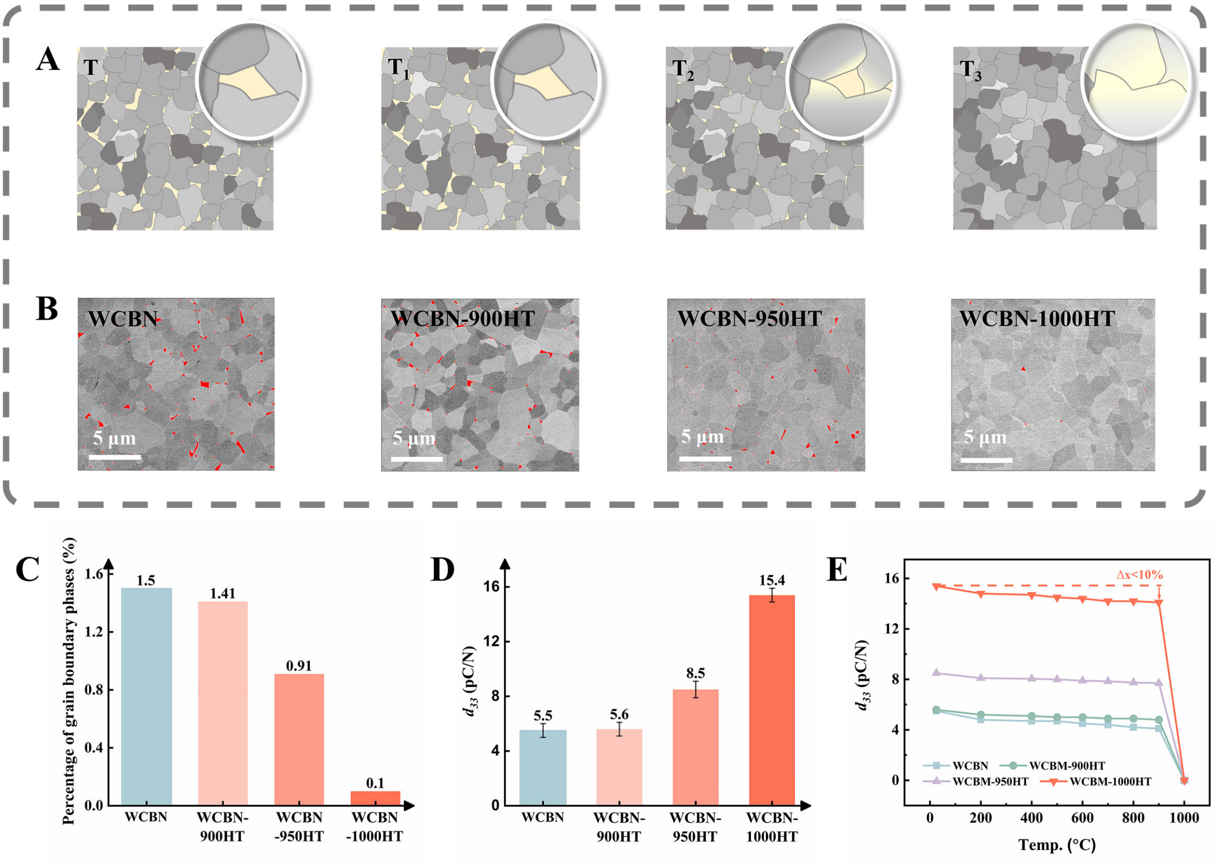

Figure 3. (A) Schematic illustration of grain boundary phase transformation. (B) ECCI images after heat treatment at different temperatures (the secondary phase indicated with RED). (C) The secondary phase area of the grain boundary after heat treatment at different temperatures. (D) The change in the d_{33} after heat treatment at different temperatures, and (E) the thermal depolarization behavior for the WCBN, WCBN-900HT, WCBN-950HT, and WCBN-1000HT ceramics.

Figure 4A and B shows the domain switching behaviors of WCBN and WCBN-1000HT ceramics using *ex-situ* electric field X-ray diffraction (XRD). As the electric field increased, the (020) peak intensity of WCBN-1000HT ceramics gradually decreased, which resulted from domain rotation toward the (100) direction[36]. In contrast, WCBN ceramics show negligible changes. This phenomenon was further quantified by the intensity ratio of the (200) and (020) peaks in Figure 4C under an electric field of 16 kV/mm, where the $I_{(200)}/I_{(020)}$ ratio of WCBN-1000HT ceramics reached 5.26, significantly higher than the value of 1.55 observed in WCBN ceramics. To further verify domain switching at the microscopic scale, piezoresponse force microscopy (PFM) measurements were performed under varying DC tip biases. Figure 4D shows that no significant domain switching occurs in WCBN ceramics when a voltage is applied. By comparison, WCBN-1000HT ceramics displayed significantly enhanced switching behavior, with a 20 V bias nearly achieving complete switching [Figure 4E].

Notably, domain structure evolution before and after heat treatment was additionally investigated to determine its impact on piezoelectric properties. Figure 5A-D displays representative ferroelectric domain images of WCBN and WCBN-1000HT ceramics, along with the corresponding selected area electron diffraction patterns. By calibrating the diffraction patterns of domains A-D, their zone axes were identified as [100] for A and C, and [010] for B and D, respectively. Since these zone axes are perpendicular to each other, it can be inferred that both correspond to 90° domain walls. PFM phase images further confirm that both samples exhibit typical "island-shaped" domain structures [Figure 4D and E][33,37]. In summary, the enhancement of piezoelectric properties after high-temperature treatment is due to the reduction of grain boundary segregation, which facilitates domain switching, rather than changes in domain configuration.

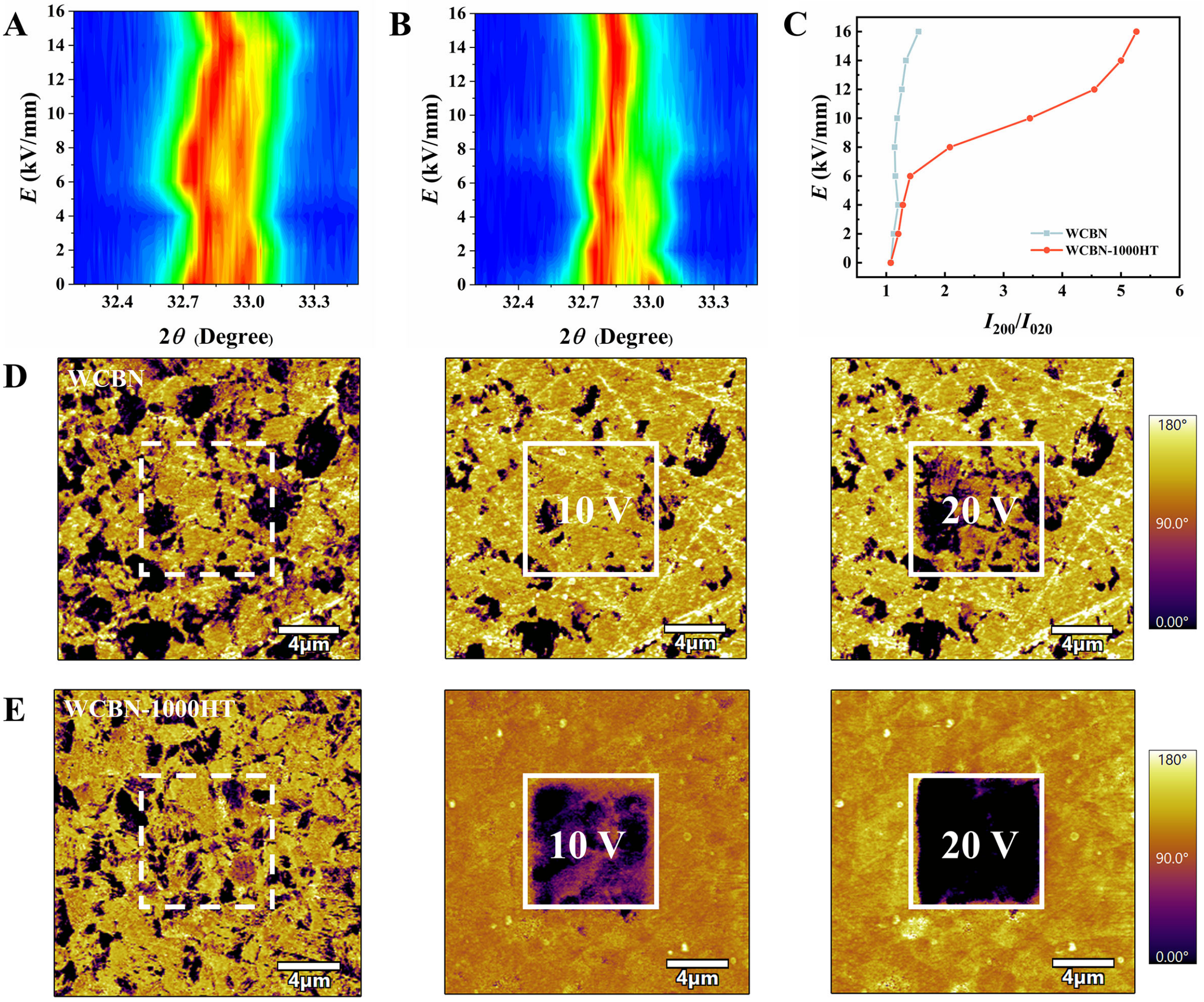

Figure 4. *Ex-situ* electric field XRD patterns of (A) WCBN and (B) WCBN-1000HT ceramics. (C) I_{200}/I_{020} of the WCBN and WCBN-1000HT ceramics under *ex-situ* electric field. PFM phase images of the (D) WCBN and (E) WCBN-1000HT ceramics were measured under voltages of 10 and 20 V.

So one question could be put forward: how does grain boundary segregation specifically inhibit domain switching? Up to now, three mechanisms have been reported: (1) oxygen vacancy pinning of domain walls[38,39]; (2) influence of high-resistivity/low-capacitor second phase on the poling electric field distribution[40]; and (3) stress-induced hindrance of domain wall motion[41,42].

X-ray photoelectron spectroscopy (XPS) was initially employed to analyze oxygen vacancy concentration changes in both WCBN and WCBN-1000HT ceramics. The O1s peaks were analyzed using XPS peak processing software. It was found that the oxygen vacancies and lattice oxygen in WCBN and WCBN-1000HT ceramics remained essentially unchanged, with values ranging between 0.21 and 0.22, suggesting that the influence of oxygen vacancies on domain switching can be disregarded [Supplementary Figure 5]. Furthermore, variations in the d_{33} after heat treatment under different atmospheres further support this conclusion [Figure 5E]. Specifically, the d_{33} remained essentially unchanged after annealing in air, N_2, and O_2 atmospheres. Figure 5F and G present the variations in resistivity and capacitance of WCBN, WCBN-900HT, WCBN-950HT, and WCBN-1000HT ceramics. The reduction of

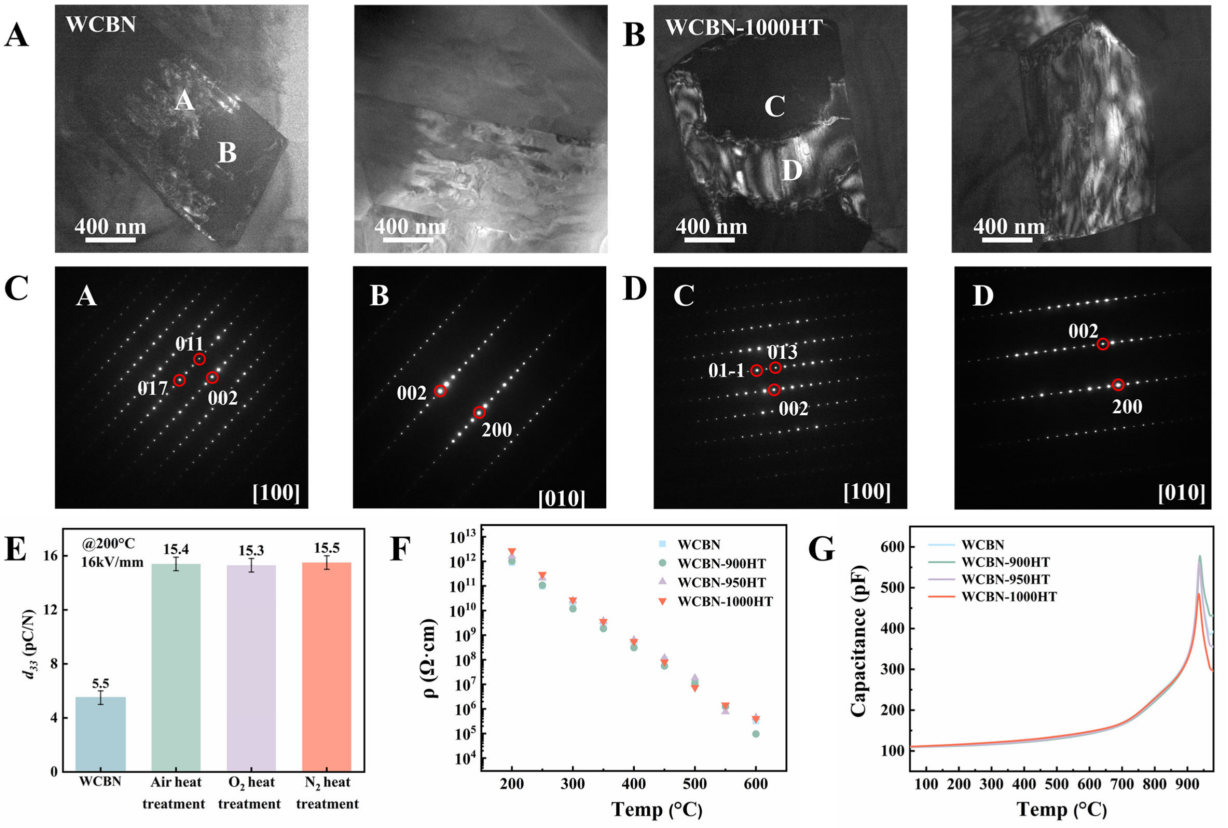

Figure 5. (A) TEM dark field images of WCBN ceramics. (B) TEM dark field images of WCBN-1000HT ceramics. (C) The diffraction patterns corresponding to A and B points in the (A). (D) The diffraction patterns corresponding to C and D points in the (B). (E) d_{33} after 1,000 °C heat treatment in different atmospheres. (F) Temperature-dependent DC resistivity. (G) Temperature-dependent capacitance.

grain boundary segregation following high-temperature treatment had minimal impact on the resistivity and capacitance, indicating that the resistivity and capacitance properties of the secondary phase at the grain boundary are similar to those of the primary phase, resulting in the maintenance of a stable distribution of the poling electric field.

In this case, considering the lattice mismatch between the secondary phase and the main phase, the hindrance to domain switching in the present work may originate from the resulting internal stresses[43,44]. As shown in Figure 6A, synchrotron XRD analysis reveals a distinct (113) diffraction peak in WCBN ceramics, which does not belong to the primary phase but rather to the secondary Bi_2WO_6 phase. Consistent with ECCI results, the secondary phase disappeared after heat treatment at 1,000 °C. Rietveld refinement calculations yield the lattice parameters of the primary and secondary phases (primary phase: a = 5.472 Å, b = 5.442 Å, c = 24.849 Å; second phase: a = 5.457 Å, b = 5.431 Å, c = 16.274 Å); the evident lattice mismatch between the two phases is expected to introduce significant compressive stress within the primary phase [Supplementary Figures 6 and 7].

High-resolution XRD (HR-XRD) and high-resolution TEM (HR-TEM) were used to analyze the internal stress of WCBN and WCBN-1000HT ceramics from macroscopic and microscopic perspectives, respectively. Figure 6B and C shows the (2210) peak of WCBN and WCBN-1000HT ceramics at different incident angles (φ = 0°, 180°; ψ = 0°, 15°, 30°, 45°). The macroscopic stress was calculated using the least-squares fitting method. The results show that the macroscopic stress in WCBN-1000HT ceramics (-184.3 ± 57.3 MPa, compressive stress) is significantly lower compared to WCBN ceramics (-268.2 ± 56.2 MPa, compressive

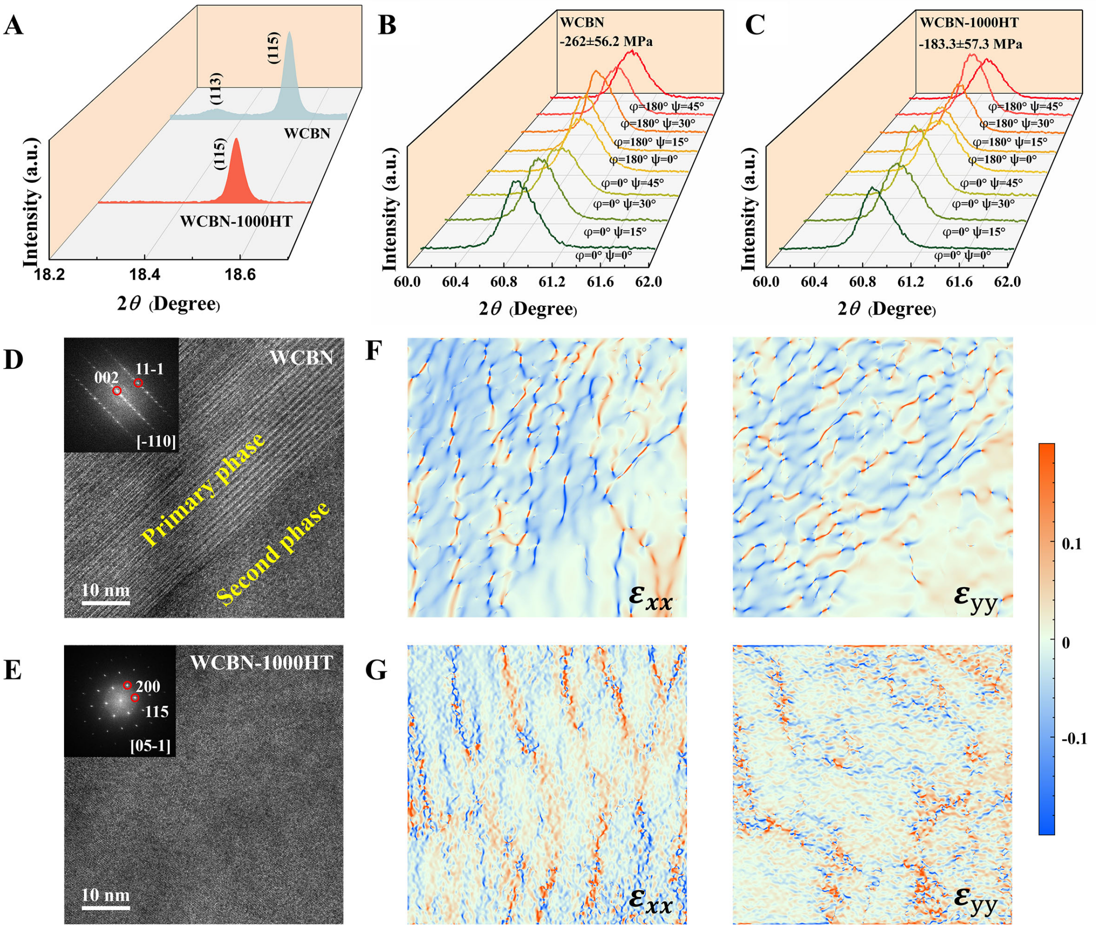

Figure 6. (A) Synchrotron XRD image. HR-XRD of (B) WCBN and (C) WCBN-1000HT ceramics at different incident angles. (D) HR-TEM of WCBN ceramics. (E) HR-TEM of WCBN-1000HT ceramics. (F) The GPA mapping of ε_{xx} and ε_{yy} corresponding to (D). (G) The GPA mapping of ε_{xx} and ε_{yy} corresponding to (E).

stress). Geometric phase analysis (GPA) is a powerful image-based technique for measuring strain, and its fundamental principle involves calculating and visualizing the deviation of a local lattice from a reference lattice derived from the corresponding electron diffraction pattern[45]. Figure 6D and E shows the HR-TEM images of WCBN and WCBN-1000HT ceramics, respectively. A two-phase structure can be observed in WCBN ceramics, where the primary phase exhibits significant compressive strain due to lattice mismatch [Figure 6F], consistent with previous assumptions. In contrast, only the primary phase is observed in WCBN-1000HT ceramics, accompanied by a significant reduction in compressive strain [Figure 6G], consistent with the HR-XRD findings.

Due to the mechanical distortion of the ferroelectric unit cell, the polarization direction of domains in piezoelectric ceramics can also be reoriented through stress-driven ferroelastic switching[46]. As shown in Figure 7A, in bismuth-layered ceramics, spontaneous polarization primarily occurs in the a-b plane[30]. When compressive stress is applied perpendicular to the a(b)-c plane, the polarization vector tends to align along the c-axis. This occurs because spontaneous polarization prefers to be perpendicular (or parallel) to compressive (or tensile) stress. In this case, compressive stress acts as a resistance, which hinders the polarization vector from switching within the a-b plane under an applied electric field. To further understand the impact of stress on domain switching, phase-field simulations were carried out to illustrate the evolution of domain structures and polarization vectors in WCBN and WCBN-1000HT ceramics under multi-field coupling conditions (refer to Supplementary Table 1 for the Landau coefficients). One thing that

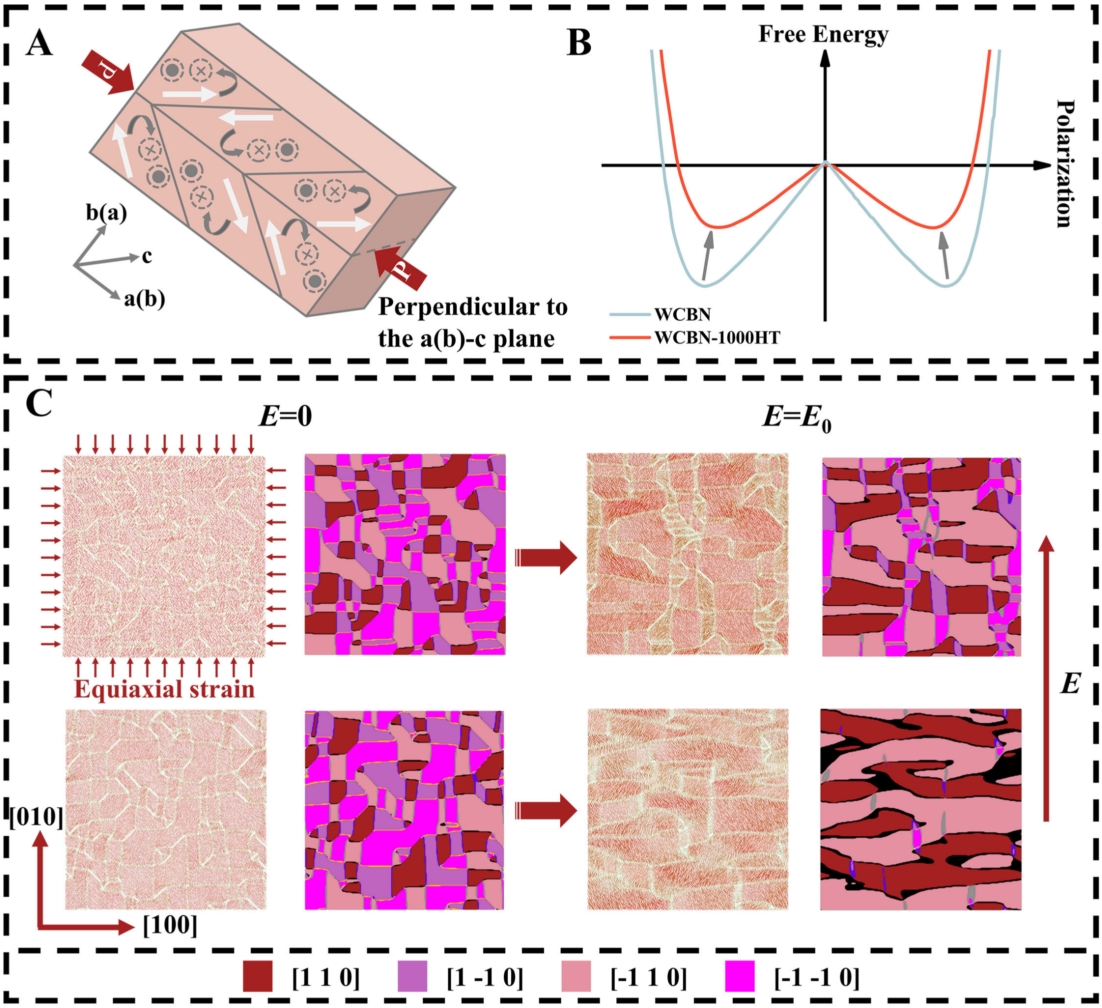

Figure 7. Phase-field simulations of WCBN and WCBN-1000HT ceramics: (A) The change of domain structure under stress. (B) Schematics of free energy *vs*. polarization. (C) Evolution of domain structure and polarization vector under multi-field coupling.

should be kept in mind is that this study only considers the internal stress caused by lattice mismatch in the a-b plane. This is because the lattice mismatch along the c-axis is relatively large, which would significantly increase the strain energy of the system and lead to structural instability[47,48]. WCBN and WCBN-1000HT are subjected to different external field conditions: both are exposed to a predefined electric field E_0 along the [010] direction, while WCBN additionally experiences an isotropic strain of -0.1 (representing residual compressive stress). The Landau free energy curves indicate that, due to the release of compressive stress, WCBN-1000HT successfully lowers the domain switching energy barrier, facilitating a smoother switching pathway [Figure 7B]. Figure 7C illustrates the evolution of domain structures and polarization vectors in WCBN and WCBN-1000HT. In the absence of an external electric field, their initial domain configurations are highly similar, which aligns with the PFM observations in Figure 4D and E. Upon the application of an electric field along the [010] direction, the polarization vectors undergo reorientation, transitioning from the initial [1-10] and [-1-10] directions to [110] and [-110]. Furthermore, it is noteworthy that WCBN retains a considerable number of polarization vectors that fail to reorient along the electric field direction compared to WCBN-1000HT (see Supplementary Figure 8 for magnified details). This confirms that the internal stress induced by grain boundary segregation hinders domain switching under the applied electric field, thereby affecting the piezoelectric properties.

The evolution of domain structures and polarization vectors under a higher applied electric field was also simulated [Supplementary Figure 9]. When the electric field strength increases to $2E_0$, the polarization vectors in WCBN, originally oriented along the [1-10] and [-1-10] directions, almost completely switch to the [110] and [-110] directions, whereas those in WCBN-1000HT remain largely unchanged. Encouragingly, this phenomenon is also confirmed at the macroscopic level through the piezoelectric coefficient d_{33}. Under a higher poling electric field (> 16 kV/mm), the d_{33} of WCBN ceramics reaches a maximum of 8.6 pC/N at 26 kV/mm, owing to further polarization vector reorientation. In contrast, the d_{33} of WCBN-1000HT ceramics remains nearly unchanged, increasing slightly to 15.5 pC/N [Supplementary Table 2]. Based on the above phenomena, we believe that the d_{33} of WCBN ceramics can be raised to the same level as that of WCBN-1000HT ceramics under the action of a strong electric field if the dielectric breakdown is not taken into account. This further demonstrates that grain boundary segregation primarily inhibits domain switching under the applied electric field.

CONCLUSIONS

In summary, by optimizing the solid-phase reaction method, we have successfully obtained WCBN ceramics with excellent fracture toughness (2.73 MPa m$^{1/2}$ at 25 °C and 2.4 MPa m$^{1/2}$ at 600 °C). More importantly, we have elucidated the influence of grain boundary segregation on the piezoelectric properties of bismuth layer-structured ceramics and demonstrated how it can be mitigated at the microscale. Through multiscale structural characterization and phase-field simulations, we found that improper grain boundary segregation suppresses domain switching due to internal stress arising from lattice mismatch with the primary phase. Furthermore, we designed a novel poling process to tailor the grain boundary segregation state in WCBN ceramics, successfully enhancing the piezoelectric coefficient by 180% and achieving 15.4 pC/N. We believe this work unlocks an unexplored pathway for designing BLSPs with both high piezoelectric and mechanical performance, and in principle, extends this strategy to other piezoelectric material systems.

DECLARATIONS

Acknowledgments

The authors sincerely thank Ms. Hongyu Li and Ms. Xiaolin Tai for their help in the testing work, which greatly facilitated the smooth progress of this research.

Authors' contributions

Conception and design of the study: Zhou, Y.; Zhou, Z.
Data acquisition and analysis: Zhou, Y.; Zhang, Y.; Huang, J.; Liu, R.; Fu, Z.; Zhou, Z.
Data interpretation: Xu, F.; Shen, Z.; Zhou, Z.
Manuscript writing and revision: Zhou, Y.; Zhang, Y.; Huang, J.; Liu, R.
Supervision: Liang, R.; Zhou, Z.

Availability of data and materials

The raw data supporting the findings of this study are available within this Article and its Supplementary Materials. Further data are available from the corresponding authors upon reasonable request.

AI and AI-assisted tools statement

Not applicable.

Financial support and sponsorship

This work was supported by the National Key R&D Program of China (Grant No. 2022YFB3204000).

Conflicts of interest

All authors declared that there are no conflicts of interest.

Ethical approval and consent to participate

Not applicable.

Consent for publication

Not applicable.

Copyright

Supplementary Materials

Supplementary Materials

REFERENCES

1. Desu, S. B.; Payne, D. A. Interfacial segregation in perovskites: IV, internal boundary layer devices. *J. Am. Ceram. Soc.* **1990**, *73*, 3416-21. DOI
2. Yan, M. F.; Rhodes, W. W. Preparation and properties of TiO_2 varistors. *Appl. Phys. Lett.* **1982**, *40*, 536-7. DOI
3. Seaton, J.; Leach, C. Direct measurement of electrical and compositional inhomogeneities in PTC thermistors. *J. Eur. Ceram. Soc.* **2004**, *24*, 1217-20. DOI
4. Sepehri-Amin, H.; Ohkubo, T.; Shima, T.; Hono, K. Grain boundary and interface chemistry of an Nd-Fe-B-based sintered magnet. *Acta. Mater.* **2012**, *60*, 819-30. DOI
5. Li, W.; Ohkubo, T.; Hono, K. Effect of post-sinter annealing on the coercivity and microstructure of Nd-Fe-B permanent magnets. *Acta. Mater.* **2009**, *57*, 1337-46. DOI
6. Zhang, G.; Chen, G.; Panwisawas, C.; et al. First-principles study of oxygen segregation and its effect on the embrittlement of molybdenum symmetrical tilt grain boundaries. *Acta. Mater.* **2023**, *261*, 119387. DOI
7. Kinoshita, T.; Munekawa, S. Effect of grain boundary segregation on thermal conductivity of hot-pressed silicon carbide. *Acta. Mater.* **1997**, *45*, 2001-12. DOI
8. Hu, J.; Chen, S.; Wang, L. A new insect-scale piezoelectric robot with asymmetric structure. *IEEE. Trans. Ind. Electron.* **2023**, *70*, 8194-202. DOI
9. Yin, Y.; Zhao, P.; Xu, X.; et al. Piezoelectric analgesia blocks cancer-induced bone pain. *Adv. Mater.* **2024**, *36*, e2403979. DOI
10. Cao, W.; Xie, S.; Liu, Y.; et al. Shear stress-triggered theranostic nanoparticles for piezoelectric-fenton-photodynamic thrombolysis and endogenous thrombus imaging. *Adv. Funct. Mater.* **2024**, *34*, 2312866. DOI
11. Zheng, T.; Wu, J.; Xiao, D.; Zhu, J. Recent development in lead-free perovskite piezoelectric bulk materials. *Prog. Mater. Sci.* **2018**, *98*, 552-624. DOI
12. Wei, H.; Wang, H.; Xia, Y.; et al. An overview of lead-free piezoelectric materials and devices. *J. Mater. Chem. C.* **2018**, *6*, 12446-67. DOI
13. Xie, S.; Xu, Q.; Chen, Q.; Zhu, J.; Wang, Q. Realizing super-high piezoelectricity and excellent fatigue resistance in domain-engineered bismuth titanate ferroelectrics. *Adv. Funct. Mater.* **2024**, *34*, 2312645. DOI
14. Li, F.; Lin, D.; Chen, Z.; et al. Ultrahigh piezoelectricity in ferroelectric ceramics by design. *Nat. Mater.* **2018**, *17*, 349-54. DOI
15. Song, A.; Liu, Y.; Feng, T.; et al. Simultaneous enhancement of piezoelectricity and temperature stability in KNN-based lead-free ceramics via layered distribution of dopants. *Adv. Funct. Mater.* **2022**, *32*, 2204385. DOI
16. Zou, J.; Song, M.; Zhou, X.; et al. Enhancing piezoelectric coefficient and thermal stability in lead-free piezoceramics: insights at the atomic-scale. *Nat. Commun.* **2024**, *15*, 8591. DOI PubMed PMC
17. Xiao, W.; Chen, Z.; Liu, X.; et al. Well-balanced performance achieved in PZT piezoceramics via a multiscale regulation strategy. *Mater. Horiz.* **2024**, *11*, 5285-94. DOI
18. Zheng, M.; Hou, Y.; Ge, H.; Zhu, M.; Yan, H. Effect of NiO additive on microstructure, mechanical behavior and electrical properties of 0.2PZN-0.8PZT ceramics. *J. Eur. Ceram. Soc.* **2013**, *33*, 1447-56. DOI
19. Fang, W.; Wu, J.; Qi, H.; et al. Synergy ascension of Piezoresponse and curie temperature in bismuth-layered ceramics via defect engineering. *Acta. Mater.* **2025**, *293*, 121108. DOI
20. Wu, J.; Ma, X.; Zhou, D.; et al. High-entropy high-temperature high-piezoelectricity ceramics. *Adv. Mater.* **2025**, *37*, e2419134. DOI
21. Subbarao, E. C. Crystal chemistry of mixed bismuth oxides with layer-type structure. *J. Am. Ceram. Soc.* **1962**, *45*, 166-9. DOI
22. Li, Y.; Liu, Y.; Öchsner, P.; et al. Temperature dependent fracture toughness of KNN-based lead-free piezoelectric ceramics. *Acta. Mater.* **2019**, *174*, 369-78. DOI
23. Yilmaz, E. D.; Mgbemere, H. E.; Özcoban, H.; Fernandes, R. P.; Schneider, G. A. Investigation of fracture toughness of modified (KxNa1−x)NbO3 lead-free piezoelectric ceramics. *J. Eur. Ceram. Soc.* **2012**, *32*, 3339-44. DOI

24. Xi, K.; Hou, Y.; Yu, X.; Zheng, M.; Zhu, M. Excellent power generation and enhanced mechanical properties in PPT-structured Pb-free piezoceramics with ZrO_2 inclusions. *J. Mater. Chem. C.* **2022**, *10*, 12359-66. DOI
25. Huang, J.; Yao, M.; Lin, J.; Yao, X. Enhanced mechanical properties and excellent electrical properties of PZT piezoelectric ceramics modified by YSZ. *Mater. Lett.* **2022**, *307*, 131006. DOI
26. Zhang, Z.; Yang, B.; Gu, W.; et al. Significantly toughened PZT-based piezoelectric ceramics simultaneously keeping excellent electrical properties via incorporating trace amount of yttria-partially-stabilized zirconia. *Ceram. Int.* **2022**, *48*, 35614-20. DOI
27. Wang, D.; Cao, M.; Yuan, J.; et al. Enhanced piezoelectric and ferroelectric properties of Nb_2O_5 modified lead zirconate titanate-based composites. *J. Am. Ceram. Soc.* **2011**, *94*, 647-50. DOI
28. Chen, Y.; Miao, C.; Xie, S.; et al. Fracture behaviors and ferroelastic deformation in W/Cr Co-Doped $Bi_4Ti_3O_{12}$ ceramics. *J. Am. Ceram. Soc.* **2016**, *99*, 2103-9. DOI
29. Jones, J. L.; Hoffman, M. R-curve and stress-strain behavior of ferroelastic ceramics. *J. Am. Ceram. Soc.* **2006**, *89*, 3721-7. DOI
30. Luo, X.; Wang, M.; Yuan, X.; et al. Piezoelectricity in excess of 30 pC N^{-1} with a high Curie temperature of 950 °C in strongly textured $CaBi_2Nb_2O_9$ ceramics. *J. Mater. Chem. A.* **2025**, *13*, 2121-30. DOI
31. Long, C.; Xu, A.; Su, Z.; Ren, W.; Liu, L.; Ding, X. Achieving outstanding comprehensive performance with high piezoelectricity in $CaBi_2Nb_2O_9$-based high-temperature piezoelectric ceramics via multi-field coupling strategy. *J. Materiomics.* **2025**, *11*, 100990. DOI
32. Chen, N.; Wang, F.; Yang, X.; et al. Improved piezoelectric performance in CBN-based ceramic through triple-doping (Li, Bi, Ce) strategy. *J. Eur. Ceram. Soc.* **2024**, *44*, 116788. DOI
33. Chen, J. N.; Pei, X. Z.; Liu, H. T.; et al. Superior piezoelectric performance in textured $CaBi_2Nb_2O_9$ ferroelectric ceramics through rare-earth gadolinium doping and spark plasma sintering. *ACS. Appl. Mater. Interfaces.* **2024**, *16*, 60511-20. DOI
34. Wang, J.; Shu, W.; Shimada, T.; Kitamura, T.; Zhang, T. Role of grain orientation distribution in the ferroelectric and ferroelastic domain switching of ferroelectric polycrystals. *Acta. Mater.* **2013**, *61*, 6037-49. DOI
35. Li, H.; Wu, B.; Lin, C.; et al. Microscopic origin and relevant grain size effect of discontinuous grain growth in $BaTiO_3$-based ferroelectric ceramics. *J. Mater. Sci. Technol.* **2023**, *164*, 119-28. DOI
36. Xie, X.; Zhou, Z.; Gao, B.; Zhou, Z.; Liang, R.; Dong, X. Ion-pair engineering-induced high piezoelectricity in $Bi_4Ti_3O_{12}$-based high-temperature piezoceramics. *ACS. Appl. Mater. Interfaces.* **2022**, *14*, 14321-30. DOI
37. Zhu, K.; Song, B.; Ge, G.; et al. Construction of multi-domain coexistence enhanced piezoelectric properties of $Bi_{0.5}Na_{0.5}TiO_3$-based thin films. *J. Eur. Ceram. Soc.* **2021**, *41*, 6456-64. DOI
38. Zhang, R.; Zhao, Y.; Yang, B.; Zhao, S. Inhibition of oxygen vacancy derived from donor doping in relaxor ferroelectric films for improving dielectric energy storage. *J. Phys. Chem. C.* **2024**, *128*, 4395-403. DOI
39. Zhang, J.; Wen, Y.; Hao, M.; et al. Enhanced properties of KNLN-BZ lead-free piezoelectric ceramics via three-step sintering. *J. Mater. Sci. Mater. Electron.* **2021**, *32*, 19778-85. DOI
40. Zhang, Y.; Roscow, J.; Lewis, R.; et al. Understanding the effect of porosity on the polarisation-field response of ferroelectric materials. *Acta. Mater.* **2018**, *154*, 100-12. DOI
41. Xia, F.; Yao, X. Postsintering annealing induced extrinsic dielectric and piezoelectric responses in lead-zinc-niobate-based ferroelectric ceramics. *J. Appl. Phys.* **2002**, *92*, 2709-16. DOI
42. Achuthan, A.; Sun, C. T. Domain switching in ferroelectric ceramic materials under combined loads. *J. Appl. Phys.* **2005**, *97*, 114103. DOI
43. Liu, Y.; Fan, J.; Qi, X.; Shen, B.; Zhang, R.; Yao, K. Adaptive ferroelectric states in KNN-based piezoceramics: Unveiling the mechanism of enhancing piezoelectric properties through multiple phase boundary engineering. *Nano. Energy.* **2024**, *128*, 109972. DOI
44. Groppi, C.; Maspero, F.; Asa, M.; et al. Spontaneous pattern of orthogonal ferroelectric domains in epitaxial KNN films. *J. Appl. Phys.* **2023**, *134*, 204102. DOI
45. Zhao, C.; Xing, Y.; Bai, P.; Hou, J.; Dai, X. Quantitative measurement of deformation field around low-angle grain boundaries by electron microscopy. *Phys. B. Condens. Matter.* **2008**, *403*, 1838-42. DOI
46. Xie, K.; Peng, Q.; Li, Y.; Tan, C. Poling lead zirconate titanate ceramics with the assistance of stress. *Ceram. Int.* **2023**, *49*, 13339-46. DOI
47. Kikuchi, T. Stability of layered bismuth compounds in relation to the structural mismatch. *Mater. Res. Bull.* **1979**, *14*, 1561-9. DOI
48. Rao, C. N. R. Intergrowth structures in inorganic solids: a new class of materials. *Bull. Mater. Sci.* **1985**, *7*, 155-78. DOI